High S and high CO2 contents in haplokimberlite: An experimental and Raman spectroscopic study

Yann Morizet, Chloé Larre, Ida Di Carlo, Fabrice Gaillard

High S and high CO_2 contents in haplokimberlite: An experimental and Raman spectroscopic study

Yann Morizet[1*], Chloé Larre[1], Ida Di Carlo[2], Fabrice Gaillard[2]

(1) Université de Nantes, Nantes Atlantique Universités, Laboratoire de Planétologie et Géodynamique de Nantes (LPG), UMR CNRS 6112, 2 rue de la Houssinière, 44322 NANTES (France)

(2) CNRS/INSU-Université d'Orléans – BRGM, UMR 7327, Institut des Sciences de la Terre d'Orléans, 1A rue de la Férollerie, 45071, Orléans, France

Corresponding author: Yann Morizet

Postal address:

Laboratoire de Planétologie et Géodynamique de Nantes (LPG Nantes), UMR-CNRS 6112, Université de Nantes.

2 rue de la Houssinière, 44322 Nantes Cedex (FRANCE)

phone: +33 (0) 2 5112 5491

fax: +33 (0) 2 5112 5268

*E-mail: yann.morizet@univ-nantes.fr

Abstract

Sulfur is an important element present in natural kimberlites and along with CO_2, S can play a role in the kimberlite degassing. We have investigated experimentally the change in S content and CO_2 solubility in synthetic kimberlitic melts in response to a range of pressure (0.5 to 2.0 GPa) and temperature (1500°C to 1525°C). Several initial S concentrations were investigated ranging from 0 to 24000 ppm. The dissolved CO_2 and S were determined by Raman spectroscopy and Electron Probe Micro-Analyses.

Under the investigated oxidizing conditions (ΔFMQ+1), S is dissolved in the glass only as S^{6+} forming sulfate molecular groups (SO_4^{2-}). The measured S concentration in the glasses increases from 2900 to 22000 ppm. These results suggest that the experimental conditions were below saturation with respect to S and that the S solubility is higher than 22000 ppm for kimberlitic melts; regardless of the experimental conditions considered here.

CO_2 is dissolved as CO_3^{2-} molecular groups. The CO_2 solubility ranges from 3.0 to 11.3 wt% between 0.5 and 2.0 GPa. CO_2 solubility is not affected by the presence of S; which suggests that SO_4^{2-} and CO_3^{2-} clusters have two distinct molecular environments not interacting together. This result implies that both CO_2 and S are efficiently transported by kimberlitic melt from the upper mantle towards the atmosphere.

Number of words: 214

Keywords: kimberlite, CO_2 and S dissolution, degassing

INTRODUCTION

Volatiles are ubiquitous components in kimberlites. In particular, CO_2 (and to a lesser extent H_2O) has been shown to be an important volatile species involved in the dynamic and geochemistry of kimberlitic melts (Dawson 1971). Natural kimberlites exhibit relatively high CO_2 and H_2O content (Kjarsgaard et al. 2009); and experimental studies have shown that CO_2 solubility can be as high as 20 wt% in kimberlitic glasses synthesized under mantle pressure conditions (Brey and Ryabchikov, 1994; Girnis et al., 2005). Under lower crustal pressure conditions H_2O solubility is comparable to the H_2O solubility observed in basalts (Moussallam et al. 2016). Up to now, the potentiality for sulfur (S) to play a significant role in kimberlitic melt has not been explored experimentally. However, S is an important volatile element involved in various magmatic systems and especially in alkaline magmas (Bailey and Hampton 1990; Brooker et al. 2011).

Sulfur in kimberlites - the present state of knowledge

Early work by Dawson (1980) gives a range of S from 200 to 8800 ppm in kimberlites from Western Australia; later, Boctor and Meyer (1982) showed the presence of sulfide minerals in kimberlite from Green Mountain. These sulfides were suspected to be the products of sulfurization process associated with serpentine. In particular, sulfides are often found as inclusions in kimberlitic diamonds (Pearson et al. 1996, 1998; Sobolev et al. 1997). The measured sulfide composition exhibits various Ni content and two groups of sulfides are defined: E-type with less than 10 wt% Ni and P-type with more than 14 wt% (Deines and Harris 1995). Since the work of Boctor and Meyer (1982), many more studies indicate that sulfides are ubiquitous mineral phase in natural kimberlites (e.g. Mitchell 1986; Griffin et al. 2002; Kopylova et al. 2007). These observations witness that S is an important element involved in the geochemistry of kimberlites.

Recent study by Kitayama et al. (2017) reported relatively high S concentrations in Udachnaya-East kimberlitic glass (up to 0.5 wt% S) in association with both sulfates and sulfides minerals. The S isotopic signature (i.e. $\delta^{34}S$) in Udachnaya-East kimberlites reveals that part of this S is magmatic in origin with $\delta^{34}S_{Sulfide}$ = -1.4 ‰. This value is totally consistent with the $\delta^{34}S$ isotopic signature from the mantle (0 ‰, Chaussidon et al. 1987; Eldridge et al. 1991; -1.2 to -1.5 ‰, Labidi et al. 2013); and is also consistent with measurement of $\delta^{34}S$ in sulfide from peridotitic inclusions in diamonds (Rudnick et al. 1993). Recent investigation by Bataleva et al. (2013) demonstrates that sulfides are produced by desulfation process from crystalline sulfates. Evidence so far suggests that the mantle magmatic source of the kimberlitic melts is enriched with respect to S and that the recovered sulfides in natural kimberlites can result from a complex mechanism involving sulfates in the mantle.

Sulfur and CO_2 behavior in high pressure silicate melts

The CO_2 or S solubility in silicate melt is currently well-apprehended as a function of intensive conditions. The CO_2 solubility in silicate melt shows a positive correlation with pressure and a slight negative correlation with temperature (Thibault and Holloway 1994; Dixon et al. 1995; Brooker et al. 1999; Morizet et al. 2002). Decreasing the fO_2 conditions induces a decrease in the CO_2 solubility in silicate melt owing to the lower thermodynamic activity of CO_2 in the fluid phase (Pawley et al. 1992; Morizet et al. 2010; Wetzel et al. 2013). For S, there is a strong positive effect of temperature on S solubility (O'Neill and Mavrogenes 2002; Jugo et al. 2005; Scaillet and Pichavant 2005; Beermann et al. 2011). Early work (Wendlandt 1982) suggested that pressure has a negative effect on the S solubility. Redox conditions play a major role on the S solubility: the S solubility in silicate melt is lower under reducing conditions (i.e. low fO_2) than under oxidizing conditions (Jugo et al. 2005). Furthermore, S solubility exhibits a non-monotonic evolution with increasing fO_2 conditions corresponding to the change in S speciation from S^{2-} to S^{6+} species (Jugo et al. 2005; Klimm et al. 2012).

The effect of silicate melt compositions on CO_2 and S solubility has been studied experimentally for decades. The most recent thermodynamic or semi-empirical models integrate the change in melt compositions to reproduce solubility data for CO_2 (Iacono-Marziano et al. 2012) and S (Zajacz and Tsay, 2019). In particular, there is a consensus from previous experimental studies that the CO_2 and S dissolution is mostly governed by the NBO/T (Brooker et al. 2001; Zajacz 2015); which corresponds to the degree of polymerization of the silicate network. The NBO/T is defined as the concentration of Non-Bridging Oxygen per Tetrahedron and is calculated on a stoichiometric basis (e.g. Mysen 1988, 1990). From the structure point of view, this parameter represents the connectivity between network forming units (i.e. tetrahedral units). Considering that Si^{4+} cation is the most important network former in silicate melts, the degree of polymerization is primarily a function of the melt SiO_2 content. A rhyolitic melt has a strongly polymerized structure whereas a kimberlitic melt is strongly depolymerized. Depolymerizing the silicate melt structure (i.e. increasing the NBO/T) will induce an increase in both CO_2 (e.g. Brooker et al. 2001; Moussallam et al. 2015) and S solubility (Zajacz 2015; Zajacz and Tsay 2019).

A great deal of effort has been made for determining the CO_2 dissolution mechanism in silicate melts. For instance, early studies (Fine and Stolper 1985; Blank and Brooker 1994; Brooker et al. 1999) showed that CO_2 dissolves in silicate melts according to the following simplified reaction:

$$CO_2^{fluid} + O^{2-melt} \rightarrow CO_3^{2-melt} \qquad (1)$$

The S dissolution mechanisms in silicate melts are more complex owing to the different S oxidation states (from S^{2-} to S^{6+}; Wilke et al. 2011; Klimm et al. 2012; Morizet et al. 2013a). Under oxidizing conditions (i.e. fO_2 > FMQ+1; Fayalite-Magnetite-Quartz), S is present as SO_2 fluid species and dissolves as S^{6+} sulfate groups (SO_4^{2-}) with the following reaction proposed by Fincham and Richardson (1954):

$$SO_2^{fluid} + \frac{1}{2}O_2^{fluid} + O^{2-melt} \rightarrow SO_4^{2-melt} \qquad (2)$$

In both reactions, O^{2-} is an oxygen species from the melt, usually a NBO taken from the silicate network tetrahedral units. The carbonate (CO_3^{2-}) and sulfate (SO_4^{2-}) molecular groups have two negative charges compensated by available network modifying cation (e.g. Na^+, K^+, Ca^{2+}, Mg^{2+}). Consequently, the dissolution of both CO_2 and SO_2 fluid species involves a strong interaction with the silicate network. It should be pointed out that the interplay in between the two chemical reactions is currently unknown and whether one chemical reaction affects the other remains to be determined. The CO_2 and S behavior are well-constrained individually; however, there is a lack of experimental investigation when mixed volatile species are present (CO_2 and S) that is a usual case in natural systems (e.g. Chiodini and Frondini 2001; Aiuppa et al. 2010). Furthermore, experimental investigation of the solubility for depolymerized melts such as kimberlites are lacking.

In the present work, we have investigated experimentally the change in CO_2 solubility in haplokimberlititc melt under high pressure and temperature conditions and in equilibrium with a mixed fluid phase CO_2-SO_2. The change in the dissolved S content is scrutinized. We have explored the dissolution mechanisms for CO_2 and S using Raman spectroscopy. We also discuss the implications of these results in term of S and CO_2 transport by kimberlitic melts.

MATERIALS AND METHODS

Starting materials

We investigated the same composition as in Morizet et al. (2017a; see Table 1); which provides S-free CO_2-bearing solubility data. As a result, the effect of S dissolution on the CO_2 solubility could be determined and comparison to S-free solubility data can be achieved. The composition (Table 1: 44.5 wt% SiO_2; 4.9 Al_2O_3; 22.8 MgO; 22.8 CaO; and 4.9 Na_2O) represents a simplified composition compared to typical natural kimberlite (e.g. Novicki et al., 2004; Becker and Le Roex, 2006); however, as shown in previous works (Brooker et al., 2001; Morizet et al., 2017a), one of the major control on volatile solubility in silicate melt is the degree of polymerization of the melt. We explore a haplokimberlite composition depolymerized in nature as expressed by the NBO/T > 2 (Brooker et al. 2001); and represents a close analogue to natural kimberlites. We prepared the

compositions from a mixture of spec pure oxides (SiO_2, Al_2O_3 and MgO), carbonate (Na_2CO_3 and $CaCO_3$) as a source of CO_2, and sulfate ($CaSO_4$) as a source of S during the experiments. Prior to the high pressure experiments, the loaded initial S is in an oxidized state (S^{6+}). We mixed the starting powder in an agate mortar under dry conditions to avoid potential contamination issues. We stored the starting material in an oven at 100°C to minimize H_2O adsorption. The starting powders contained an excess fluid phase: >17 wt% CO_2; and different initial S content: 3300, 6500, 12800 and 24000 ppm (see Table 1). We weighed the starting material into Pt capsules and we sealed the capsule by arc-welding. We checked the capsule for leakages by placing the capsule after the experiments into a hot silicon oil bath.

Experimental syntheses

We investigated pressure conditions from 0.5 to 2.0 GPa and temperature above 1500°C to make sure super-liquidus conditions were reached. The experiments were performed in an end-loaded piston-cylinder apparatus using ¾ and ½ inch talc-Pyrex assembly for high pressure experiments at 0.5-1.5 and 2.0 GPa, respectively. We used talc-Pyrex assemblies manufactured by Ceramic Substrate© company. The talc-Pyrex assembly self-imposes oxidizing conditions above FMQ+1 (Kägi et al. 2005). Those oxidizing conditions induce the presence of oxidized species only (i.e. CO_2 and SO_2) in the fluid phase. It should be pointed out that we did not conduct redox controlled experiments in which the fO_2 conditions are reducing to induce the presence of sulfide species. The Pt capsule was surrounded by a Magnorite© ceramic sleeve to avoid contact with the graphite furnace. We used the pressurization method described in Brooker et al. (1998) for the attainment of the experimental conditions: 1) pressure is increased to 0.5 GPa at room temperature, 2) temperature is increased up to 500°C, 3) pressure is increased up to the desired pressure using the automatic needle pump Stigma© at a rate of 75 bars/sec., and 4) temperature is increased at a rate of 40°C/min.. During the experiment, the temperature is monitored by a type B ($PtRh_6$-$PtRh_{30}$) thermocouple with an accuracy of ±5°C. The experiment durations were at least 3h to attain equilibrium conditions. The quench is done by cutting off the power. We applied an isobaric quench (no decompression bubbles) with an automated needle pump. The quench rate is timed at approximately 100°C/sec. in the first five hundreds °C.

The hiss at the opening of the capsules indicates that all the experiments were conducted in fluid saturated conditions. We examined the recovered samples optically and samples showing evidences of crystals were discarded. Most of the experimental charges consist in a clear glass; however, we observed that at high S content, the glass is slightly colored in brown. Examination using Secondary Electron Microscopy for these

samples did not reveal the presence of crystals (see Online Resource 1). We separated the recovered experimental charge in several aliquots for subsequent analyses.

Analytical methods

Electron Probe Micro-Analysis (EPMA)

For each sample, we embedded a glass fragment into an epoxy resin pellet, polished down to 1 µm, and coated with a thin carbon surface. We determined the major element concentrations and total S content in glasses using Electron Probe Micro-Analyses Cameca SXFive©, with 15kV and 6 nA, with 10 s peak counting time for all elements (5 s counting on the background). The standards for our analysis were wollastonite ($CaSiO_3$), corundum (Al_2O_3), albite ($NaAlSi_3O_8$), periclase (MgO), barite ($BaSO_4$). Na was analyzed first to avoid alkali loss. We conducted the analyses in defocused mode (20 µm beam diameter) to limit elemental loss. The determined glass composition is reported in Table 1 in wt%. The average glass major elements concentrations were obtained from more than 20 analyses. The standard deviation (one sigma) for each oxide is better than 0.5 wt%.

The measured glass compositions exhibit differences in the major element concentration (see Table 1) when compared to the theoretical composition. These differences are due to difference in the batch starting material. However, glass samples can be compared to each other. Furthermore, the degree of polymerization expressed as the NBO/T and calculated from stoichiometry is 1) very close to the theoretical composition and 2) comparable within each glass (see Table 1). Considering the NBO/T is a strong control on the CO_2 solubility (Brooker et al. 2001) and S solubility (Zajacz 2015; Zajacz and Tsay 2019), the slight variation in glass compositions (~0.2 in NBO/T) will not influence the volatile solubility; especially at such high CO_2 solubility and S content.

Raman spectroscopy

For each glass sample, we collected Raman spectra on a Jobin-Yvon LabRam HR Micro-Raman spectrometer equipped with a 532 nm laser wavelength. For this non-destructive method, no sample preparation is required (i.e. raw piece of glass placed on a glass slide). The laser output power is set at 100 mW without damaging the sample. We used a 1200 grating/mm corresponding to a spectral resolution of ~0.8 cm^{-1}. The acquisition time was typically 30 to 60 s with 5 to 10 repeated scans. We performed the acquisitions in a non-confocal mode with a slit aperture of 200 µm and a X50 long working distance Olympus objective. The non-confocal mode results in a large glass volume analyzed (~10 µm in depth). At least 3 spectra were obtained on different glass chips from the experimental charge to assert sample homogeneity with respect to S and CO_2 contents.

We studied the spectral range 200-1250 cm^{-1} covering the area of the silicate network, the CO_2 dissolved as CO_3^{2-} (ν_1 CO_3^{2-} ~1080 cm^{-1}; Morizet et al. 2013b) and S dissolved as SO_4^{2-} (ν_1 SO_4^{2-} ~1000 cm^{-1}; Klimm and Botcharnikov 2010). The 2500-3900 cm^{-1} frequency region was also investigated to determine the possible presence of water and reduced S species (S^{2-}; Klimm et al. 2012). The spectra were background subtracted by placing a polynomial function in the no-band areas: ~200, ~800 and above 1200 cm^{-1} (Morizet et al. 2013b).

RESULTS

Raman spectra of CO_2- and S-bearing kimberlitic glasses

Fig. 1 shows typical Raman spectra for CO_2- S-bearing haplokimberlitic glasses (Fig. 1a) and the typical deconvolution for Raman spectra showing the determined ppm S^{6+} and the wt.% CO_2 (Fig. 1b). We represent the Raman spectra in the range 775-1200 cm^{-1} corresponding to the region of interest for the studied volatile species and the glass structure. The Raman spectra shown in Fig. 1 exhibit several vibrational features that are characteristic of 1) the silicate network symmetric stretch showing a broad signal in the 800-1200 cm^{-1} range, 2) the dissolved sulfate symmetric stretch (ν_1 SO_4^{2-}) at ~1000 cm^{-1} and 3) the dissolved carbonate symmetric stretch (ν_1 CO_3^{2-}) at ~1080 cm^{-1}. The silicate network signature is a combination of several individual species called Q^n species (n representing the number of Bridging Oxygen, BO from 0 to 4; McMillan 1984; Frantz and Mysen 1995; Mysen 1999). Investigating the distribution of Q^n species is beyond the scope of this work, however, the line shape of the silicate network symmetric stretch (i.e. the distribution of Q^n species) is a function of the melt chemical composition. In depolymerized kimberlitic melts, the silicate network vibrational signature will be shifted to lower Raman shift value whereas for fully polymerized composition (e.g. rhyolitic melt) the silicate network vibrational signature will be shifted to the right and extend up to 1200 cm^{-1}.

Reduced S species such as HS^- (peak at ~2570 cm^{-1}; Klimm et al. 2012) have not been observed in the Raman spectra. A small amount of water has been observed with a Raman signature at ~3500 cm^{-1}. The H_2O peak intensity is small suggesting that H_2O is present under low concentration (<0.3 wt%). The presence of H_2O in experimental charge from high pressure piston-cylinder experiments is almost unavoidable. Although we took precautions for preparing the starting materials, H_2O is present as moisture adsorbed to the powder.

In Fig. 1a, the spectra have been scaled to the same intensity for the ν_1 CO_3^{2-} located at ~1080 cm^{-1}. The dissolved CO_2 content is correlated to the ratio between the intensity (or area) of the ν_1 CO_3^{2-} and the one for the silicate network (Morizet et al. 2013b). As observed in Fig. 1a, there is an apparent decrease in the intensity of the silicate network vibrational signature from HKS1-3 to HKS3-2. This observation is consistent with an

increase in the CO_2 content from HKS1-3 to HKS3-2. The increase in CO_2 content is in agreement with our current knowledge: CO_2 solubility is positively correlated to the increase in the experimental pressure (Thibault and Holloway 1994).

The intensity of the ν_1 SO_4^{2-} peak is also correlated to the amount of dissolved S as S^{6+} (Morizet et al. 2017b). As shown in Fig. 1a, HKS3-2 and HKS1-3 spectra exhibit a strong signal for ν_1 SO_4^{2-} at 1000 cm^{-1} consistent with high S content dissolved as S^{6+}. This peak is absent for HKS4-1 spectrum suggesting S is dissolved in low concentration. The peak intensity appears correlated to the initial loaded S. For instance, the HKS4-1 loaded with 3300 ppm S does not show evidence for intense ν_1 SO_4^{2-} peak; on the contrary, the HKS3-1 loaded with 24000 ppm exhibits a strong ν_1 SO_4^{2-} peak located at ~1000 cm^{-1}. It also implies a very low concentration of S in the fluid phase.

Raman spectroscopy versus EPMA for the quantification S in glasses

We used the calibration of Morizet et al. (2013b) for quantifying the CO_2 content and the calibration of Morizet et al. (2017b) for quantifying the S content dissolved as S^{6+} species. The spectrum simulation were conducted with the Origin© peak fitting package. The setup of the initial conditions for the spectrum deconvolution is critical. The peak positions for the SO_4^{2-} and CO_3^{2-} is roughly constant. The SO_4^{2-} peak position ranges from 999.0 to 1007.8 cm^{-1}; the CO_3^{2-} peak position ranges from 1082.0 to 1088.3 cm^{-1}. The silicate network species have variable position depending on the glass chemical composition and on the degree of polymerization (Morizet et al. 2013b). The Full Width at Half Maximum (FWHM) is dependent on the considered species: for SO_4^{2-} and CO_3^{2-} we used a FWHM at ~30 cm^{-1}; whereas for silicate network species, the FWHM is fixed at ~60 cm^{-1}. The lower FWHM for SO_4^{2-} and CO_3^{2-} is due to the molecular configuration of these species. The S-O and C-O bonds are not strongly perturbed by the surrounding silicate network and therefore the distribution in S-O bond length is not large. On the contrary, the tetrahedral units of the silicate network have strong interactions (i.e. strong interconnections) and the distribution in the Si-O bond length (and bond angles) is larger (Morizet et al. 2013b; 2017b).

The simulation is obtained by successively optimizing the Gaussian peak positions and FWHM. The procedure is repeated several times in order to obtain the lowest chi-squared value traducing the robustness of the fit. It should be emphasized that the simulation result shown in Fig. 1b represents only one possible solution. Error in the determination of the S content using Raman is possible owing to the important overlapping of the ν_1 SO_4^{2-} peak with the silicate network peaks. The error associated with the spectrum deconvolution is less important for

the quantification of CO_2 as the ν_1 CO_3^{2-} peak is on the right hand side of the silicate network; therefore the definition and simulation of the peak is less impacted by the presence of the silicate network vibrations.

We determined the ratio between the areas of the Gaussian peaks of the species to be quantified (i.e. ν_1 SO_4^{2-} and ν_1 CO_3^{2-} peaks) and the sum of the silicate network species (see Fig. 1b). The concentration of the species of interest (i.e. CO_2 and S^{6+}) is determined with the following equation:

$$C_i = \alpha_i \times \frac{A_i}{\sum A_{silicate\ network}} \quad (3)$$

Where C_i is the content of the i species, A_i is the area of the Gaussian peak for the i species, $\sum A_{silicate\ network}$ is the sum of the Gaussian peak area for the silicate network units, and α_i is the calibration factor for the i species: $\alpha_{SO4^{2-}} = 34371$ and $\alpha_{CO3^{2-}} = 13.5$; from Morizet et al. (2017b) and Morizet et al. (2013b), respectively. Additional simulation results are provided in the Online Resource 1. The error reported in Morizet et al. (2013b, 2017b) on the determined CO_2 and S concentrations are ±0.4 wt% and ±609 ppm, respectively. The S content is given in ppm and the CO_2 in wt% in Table 1. The error reported for CO_2 and S corresponds to the standard deviation derived from replicated measurements and therefore witnesses the homogeneity in the CO_2 and S contents within the glass. The S content in HKS4-1 could not be determined due to the extremely low concentration in S and no reliable simulation of the ν_1 SO_4^{2-} peak could be achieved.

For the presently synthesized CO_2- and S-bearing glasses, the determined range of CO_2 is 3.1 to 11.3 wt% from Raman and the S content ranges from 536 to 25507 ppm from EPMA (see Table 1). We have compared the results obtained for quantifying ppm S^{6+} from Raman spectroscopy and the total S quantification from EPMA. As shown in Table 1 and Fig. 2, we observe that the ppm S^{6+} determined with Raman is in agreement with the ppm S^{tot} determined from EPMA. It should be emphasized that different glass chips were used for the quantification of S by Raman and EPMA. It implies that possible heterogeneity in the S content within the glass experimental charge is discarded. The most important difference in the measured S content is observed for the sample with the highest S concentration (HKS3-2). There is a ~4000 ppm difference in the determined S between Raman (21296 ppm S^{6+}) and EPMA (25507 ppm S^{tot}). The EPMA method is one of the most reliable method for analyzing the S content (e.g. Clemente et al., 2004; Evans et al., 2008; Lesne et al., 2011) and therefore provides more accurate measurement of the S content. However, the measured S content in this glass cannot be above the loaded S content (24000 ppm). In that case, the EPMA analysis (25507 ppm) overestimates the S in that particular sample and the Raman determination (21296 ppm) is more representative of the actual S content in this glass. Although, as the determination of the S content using Raman spectroscopy is dependent on

the spectrum simulation (see Fig. 1b), a more important error is expected. Nevertheless, we show that both methods are in agreement with respect to S determination.

DISCUSSION

Volatile content and effect of S on CO_2 solubility

The change in the CO_2 solubility and S content as a function of pressure is reported in Fig. 3. We observe from data in Table 1 and Fig. 3 that the measured S content in the glass is very close to the initial loaded S content in the starting powder (see Table 1), suggesting that most of the experiments were conducted in undersaturated conditions with respect to S. The HKS1-2 -3 have ~11000 ppm dissolved for an initial S content of 12800 ppm; HKS4-2 has 2870 ppm S for an initial S content of 3300 ppm; and 25507 ppm S (21296 ppm using Raman spectroscopy) has been measured for HKS3-2 for an initial S content of 24000 ppm. We observe several experimental charges for which the ppm S measured by EPMA is very low in comparison to the loaded initial S. Currently, this observation is unexplained. Nevertheless, the determined high S content implies that in most of the case we did not reach the S saturation limit. Another piece of evidence is the absence of sulfate crystallization that would indicate the sulfate saturation (Li and Ripley 2009). These results also point to the fact that S is mostly dissolved in the melt; however, there is a part of the S present in the fluid phase suggesting that there is a thermodynamic equilibrium between the melt and the fluid during the experiments.

To the exception of the work of Zajacz (2015) and Jugo et al. (2005) and for oxidizing conditions, the S content in HKS3-2 (>20000 ppm S) is the highest measured so far in silicate glasses. Jugo et al. (2005) measured a maximum solubility of ~20000 ppm in basaltic glass synthesized at 1 GPa. Zajacz (2015) showed that increasing the degree of depolymerization (i.e. increasing the NBO/T) increases the S solubility. More recently, Zajacz and Tsay (2019) established a model for the S solubility that is positively correlated with the NBO/T parameter. Considering that we investigate a strongly depolymerized composition (NBO/T > 2) analogous to natural kimberlitic melts; we show that kimberlitic melts have the capacity to dissolve a large quantity of S in its silicate network structure.

The measured CO_2 solubility (up to 11.3 wt%) is below the initial CO_2 loaded in the starting material (~18 wt%) and the excess CO_2 is in the fluid phase. At 0.5 GPa, 2.9 wt% CO_2 were reported in Morizet et al. (2017a) for HK-2 and more than 3.8 wt% CO_2 are measured in presence of S: 6198, 11298 and 11979 ppm S for HKS2-3, HKS1-2 and HKS1-3, respectively. Furthermore, at 2 GPa, the CO_2 solubility is 10.9 and 11.3 wt% for S content of 25507 and 2870 ppm, respectively. We observe a gradual increase in the CO_2 solubility regardless of the S

content. This result was not anticipated and following thermodynamic consideration a decrease in the CO_2 solubility with increasing S was expected. As a result, we suggest that S does not seem to have any effect on CO_2 solubility considering that we obtain a similar CO_2 solubility for S-bearing and S-free glasses.

CO_2 solubility as a function of CO_2 fugacity in mixed CO_2-SO_2 fluid composition

During the high pressure high temperature experiments, there is a coexistence between a silicate melt and supercritical fluid phase that is a mixture of CO_2 and SO_2 owing to the oxidizing conditions. The thermodynamic calculations are performed taking into account the mixed fluid phase. We used mass balance to determine the molar fraction of each fluid species (see Table 1) such as:

$$X_{CO2}^{fl} + X_{SO2}^{fl} = 1 \qquad (4)$$

Where X is the molar fraction of the fluid species either CO_2 or SO_2. Owing to the very important difference in between the loaded CO_2 and S prior to the experiments we can reasonably approximate the molar fraction of the i species in the fluid phase with the following equation:

$$X_i^{fl} + X_i^m \approx X_i^{tot} \qquad (5)$$

Where X_i^{tot} corresponds to the molar fraction of the i species initially loaded in the experiment; X_i^{fl} and X_i^m are the molar fractions of the i species determined in the melt and in the fluid phase. It can be seen that CO_2 represents most of the fluid phase as compared to SO_2 (SO_2 is supposed to be the stable S species in the fluid under oxidizing conditions) with more than 84% CO_2 in HKS3-1 at initial conditions. The species activity in the fluid is calculated with the following:

$$a_i^{fl} = X_i^{fl} \times f_i(P,T) \qquad (6)$$

Where $f_i(P,T)$ corresponds to the fugacity of the i fluid species at the P and T conditions. The fugacity has been calculated with equation of state valid in the investigated P and T range (Holland and Powell, 1991; Shi and Saxena, 1992). The calculated f_i(P,T) for SO_2 and CO_2 are given in Table 1. We clearly observe that the activity of SO_2 in the fluid phase is extremely low in comparison to the one of CO_2 owing to the extremely low X_{SO2} in the fluid phase: at least one order of magnitude of difference in between the f_{SO2}(P,T) and the f_{CO2}(P,T).

We have reported in Fig. 4 the change in CO_2 solubility as a function of f_{CO2} for the derived fluid composition. We also have reported CO_2 solubility data from a few previous studies within the same range of pressure (i.e. f_{CO2}) and for comparable types of silicate melt compositions: Ca- and Mg-melilitite from Brooker et al. (2001); olivine melilitite from Brey and Ryabchikov (1994); olivine leucitite from Thibault and Holloway (1994); and melilitite from Morizet et al. (2017a). We observe in Fig. 4 that the CO_2 solubility measured in the

haplokimberlitic melt is intermediate between the melilitite and olivine leucitite. This behavior was anticipated. Morizet et al. (2017a) showed that increasing Mg content (i.e. decreasing Ca content) induces a decrease in CO_2 solubility for comparable degree of polymerization; therefore explaining the lower CO_2 solubility in the HKS composition as compared to the melilitite composition. The olivine leucitite composition has a lower NBO/T than HKS composition and therefore lower CO_2 solubility is expected. As inferred earlier, we clearly show that dissolving S does not influence the CO_2 solubility for kimberlitic melts. It also implies that the major control for CO_2 dissolution in a given composition is the activity of CO_2 in the fluid phase.

SO_2 and CO_2 dissolution mechanisms and implication for volatile transport by kimberlitic melt

The absence of S effect on CO_2 solubility is explained partly by the composition of the fluid phase (mainly CO_2); however, the question of the S and CO_2 dissolution mechanisms remains open. One hypothesis for explaining the absence of S effect on CO_2 solubility is that CO_2 and S have two distinct dissolution mechanisms with different surrounding cations. Recent work (Morizet et al. 2019) showed that CO_3^{2-} groups in depolymerized glasses are mostly dissolved in the surrounding of Ca^{2+} cations (and not Mg^{2+}). Currently, the cationic affinity for SO_4^{2-} groups is unknown. One hypothesis is that SO_4^{2-} groups dissolve preferentially in the surrounding of Mg^{2+} cations instead of Ca^{2+}. In that case, the local environment of CO_3^{2-}, which is mostly Ca^{2+} (or Na^+ to some extent), will not be affected or weakly affected by the dissolution of SO_4^{2-} groups.

The presented results also implies that kimberlitic melts represent a good carrier of S providing that S is present in the magmatic source. If we assume a S content in the Earth's mantle at ~200 ppm (see Palme and O'Neill, 2003 and references therein) and considering that S is an incompatible element, the high S content (>20000 ppm) measured in the haplokimberlitic melt would be obtained with ~1% partial melting that corresponds to the incipient melting (Wallace and Green 1988; Presnall and Gudfinnsson 2005; Green et al. 2010). Considering that incipient melting is the most feasible process to generate kimberlitic melts (Tappe et al. 2018); hence, our measurement of the high S content in kimberlitic melts is totally consistent.

The results demonstrate that S can be dissolved in large quantities in strongly depolymerized melts (at least 2.0 wt% S). We did not strictly reach the saturation with respect to S, further work is required in order to determine the S solubility for these melt compositions. The determined CO_2 solubility and S content in the present work also imply that the partition coefficient ($D_{m/fl}$ corresponding to the ratio between the concentrations of the element in the melt and in the fluid) of S (dissolved as S^{6+}) is by far higher than the one for CO_2. In other words S appears to be much more soluble than CO_2 in kimberlitic melts at high pressure.

The present experimental work concentrates on the high sulfate content owing to the oxidizing conditions during the experiments. This approach is not incompatible to the observed sulfides in natural kimberlites (Boctor and Meyer, 1982; Griffin et al., 2002; Katayama et al., 2017). As demonstrated by Bataleva et al. (2018), transformation from sulfates to sulfides is possible under mantle conditions and could take place into kimberlitic melts. The reactions proposed by Bataleva et al. (2018) involves several chemical reactions desulfation and sulfidation with olivine and carbon (i.e. diamond) to form pyroxenes and sulfides.

SUMMARY

Magmatic systems have often multiple volatile species (e.g. CO_2, H_2O and SO_2). Deciphering the interplay between volatiles is a key aspect for understanding volcanic degassing processes. For a synthetic kimberlitic compositions, we have conducted a series of experiment under high pressure (0.5-2.0 GPa) and high temperature (>1500°C), under oxidizing conditions, and a mixed fluid phase (CO_2 and SO_2). In the present work we show that:

- Under oxidizing conditions, S is dissolved as SO_4^{2-} molecular group. The measured S content suggests that the S solubility in low silica depolymerized composition is extremely high; and comparatively, the S partition coefficient is higher than the one for CO_2.
- The presence of S does not influence the CO_2 solubility (the opposite is also true: the presence of CO_2 does not influence S solubility). This is explained by the low thermodynamic activity of the SO_2 in the fluid phase in comparison to the one of CO_2; but also by distinct dissolution mechanisms for CO_2 to form CO_3^{2-} and SO_2 to form SO_4^{2-} molecular groups. SO_4^{2-} and CO_3^{2-} molecular groups have two distinct local environments not competing together.
- During incipient melting, low silica, strongly depolymerized kimberlitic melts have a strong transport capacity for CO_2 but also for S. It has major implications in particular for planetary bodies such as Mars for which S is recognized as a key element.
- The present results are consistent with the observation that S-bearing phases are observed as magmatic crystallization products in kimberlite magma.

Future work will concentrate on the determination of the exact SO_4^{2-} and CO_3^{2-} molecular configuration in the glass structure. In detail, determining the nature of the surrounding cations for each volatile species will be an objective to fulfill as the volatile species diffusion properties will strongly depend on the associated cations.

Acknowledgements: The authors thank the INSU CNRS, which financed the current work through the SYSTER program. The authors would like to thank the University of Orléans, the University of Nantes and the CNRS for their access to analytical facilities. We would like to thank Christoph Hauzenberger for handling our manuscript; Bruce A. Kjarsgaard and an anonymous reviewers for their fruitful comments that helped to improve our manuscript.

References:

Aiuppa A, Bertagnni A, Métrich N, Moretti R, Di Muro A, Liuzzo M, Tamburello G (2010) A model of degassing for Stromboli volcano. Earth Planet Sci Lett 295:195-204

Bailey DK, Hampton CM (1990) Volatiles in alkaline magmatism. Lithos 26:157-165

Bataleva Y, Palyanov Y, Borzdov Y (2018) Sulfide formation as a result of sulfate subduction into silicate mantle (experimental modeling under high P,T-parameters). Minerals 8:373-388

Becker M, Le Roex AP (2006) Geochemistry of South African on- and off-craton, Group I and Group II kimberlites: Petrogenesis and source region evolution. J Petrol 47:673-703

Beermann O, Botcharnikov RE, Holtz F, Diedrich O, Nowak M (2011) Temperature dependence of sulphide and sulphate solubility in olivine-saturated basaltic magmas. Geochim Cosmochim Acta, 75:7612-7631

Blank JG, Brooker RA (1994) Experimental studies of carbon dioxide in silicate melts: solubility, speciation and stable isotope behavior. In: MR Carroll and JR Holloway (eds) Volatiles in Magmas, MSA Rev Mineral 30:157-186

Boctor NZ, Meyer OA (1982) Oxide and sulphide minerals in kimberlite from Green Mountain, Colorado. In Kimberlites, Diatremes, and Diamonds: Their Geology, Petrology, and Geochemistry, Meyer HOA, Boyd FR 15 doi.org/10.1029/SP015p0217

Brey G, Ryabchikov I (1994) Carbon dioxide in strongly undersaturated melts and origin of kimberlitic magmas Neues Jahrbuch für Mineralogie H10:449–463

Brooker RA, Holloway JR, Hervig RL (1998) Reduction in piston cylinder experiments: The detection of carbon infiltration into platinum capsules. Am Mineral 83:985-994

Brooker RA, Kohn SC, Holloway JR, McMillan PF, Carroll MR (1999) CO_2 solubility, speciation and dissolution mechanisms for melt compositions along the $NaAlO_2$-SiO_2 join. Geochim Cosmochim Acta 63:3549-3565

Brooker RA, Kohn SC, Holloway JR, McMillan PF (2001) Structural controls on the solubility of CO_2 in silicate melts Part I: Bulk solubility data. Chem Geol 174:225–240

Brooker RA, Sparks RSJ, Kavanagh JL, Field M (2011) The volatile content of hypabyssal kimberlite magmas: some constraints from experiments on natural rock compositions. Bull Volc 73:959–981

Chaussidon M, Albarède F, Sheppard MF (1987) Sulphur isotope heterogeneity in the mantle from ion microprobe measurements of sulphide inclusions in diamonds. Nature 330:242-244

Chiodini G, Frondini F (2001) Carbon dioxide degassing from the Albani Hills volcanic region, Central Italy. Chem Geol 177:67-83

Clemente B, Scaillet B, Pichavant M (2004) The solubility of sulphur in hydrous rhyolitic melts. J. Petrol. 45:2171-2196

Dawson JB (1971) Advances in kimberlite geology. Earth-Sciences Rev 7:187–214

Dawson JB (1980) Kimberlites and their xenoliths. In Minerals, Rocks and Mountains, Grove TL (ed) 15, pp. 252

Deines P, Harris JW (1995) Sulfide inclusion chemistry and carbon isotopes of African diamonds. Geochim Cosmochim Acta 59:3173-3188.

Dixon JE, Stolper EM, Holloway JR (1995) An experimental study of water and carbon dioxide solubilities in Mid-Ocean Ridge basaltic liquids. Part I: calibration and solubility models. J Petrol 36:1607-1631.

Eldridge CS, Compston W, Williams IS, Harris JW, Bristow JW (1998) Isotope evidence for the involvement of recycled sediments in diamond formation, Nature 353:649-653

Evans KA, O'Neill HSC, Mavrogenes JA (2008) Sulphur solubility and sulphide immiscibility in silicate melts as a function of the concentration of manganese, nickel, tungsten and copper at 1 atm and 1400°C. Chem Geol 255:236-249.

Farrell S, Bell K, Clark I (2010) Sulfur isotopes in carbonatites and associated silicate rocks from the Superior Province Canada. Min Pet 98:209-226

Fine G, Stolper E (1985) The speciation of carbon dioxide in sodium aluminosilicate glasses. Contrib Mineral Petrol 91:105-121

Frantz JD, Mysen BO (1995) Raman spectra and structure of $BaO–SiO_2$, $SrO–SiO_2$ and $CaO–SiO_2$ melts to 1600°C. Chem Geol 121:155-176

Girnis AV, Bulatov VK, Brey GP (2005) Transition from kimberlite to carbonatite melt under mantle parameters: An experimental study. Petrology 13:1-15

Green DH, Hibberson WO, Kovács I, Rosenthal A (2010) Water and its influence on the lithosphere-asthenosphere boundary. Nature 467:448-451

Griffin WL, Spetsius ZV, Pearson NJ, O'Reilly (2002) In situ Re-Os analysis of sulfide inclusions in kimberlitic olivine: New constraints on depletion events in the Siberian lithospheric mantle. Geochem Geophys Geosyst 3:1069-1094

Haughton DR, Roeder PL, Skinner BJ (1974) Solubility of sulfur in mafic magmas. Econ Geol 69:451-467

Holland T, Powell R (1991) A Compensated-Redlich-Kwong (CORK) equation for volumes and fugacities of CO_2 and H_2O in the range 1bar-50kbar and 100-1600°C. Contrib Min Pet 109:265-273

Iacono-Marziano G, Morizet Y, Le Trong E, Gaillard F (2012) New experimental data and semi-empirical parameterization of H_2O–CO_2 solubility in mafic melts. Geochim Cosmochim Acta 97:1-23

Jugo PJ, Luth RW, Richards JP (2005) An experimental study of the sulfur content in basaltic melts saturated with immiscible sulfide or sulfate liquids at 1300°C and 10 GPa. J Petrol 46:783-798

Kägi R, Müntener O, Ulmer P, Ottolini L (2005): Piston-cylinder experiments of H_2O undersaturated Fe-bearing systems: An experimental setup approaching fO_2 conditions of natural calc-alkaline magmas. Am Mineral 90:708–717

Kitayama Y, Thomassot E, Galy A, Golovin A, Korsakov A, d'Eyrames E, Assayag N, Bouden N, Ionov D (2017) Co-magmatic sulfides and sulfates in the Udachnaya-East pipe (Siberia): A record of the redox state and isotopic composition of sulfur in kimberlites and their mantle sources. Chem Geol 455:315-330

Kjarsgaard BA, Pearson DG, Tappe S, Nowell GM, Dowall DP (2009) Geochemistry of hypabyssal kimberlites from Lac de Gras Canada: Comparisons to a global database and applications to the parent magma problem. Lithos 1125:236-248

Klimm K, Botcharnikov RE (2010) The determination of sulfate and sulfide species in hydrous silicate glasses using Raman spectroscopy. Am Mineral 95:1574–1579

Klimm K, Kohn SC, O'Dell LA, Botcharnikov RE, Smith ME (2012) The dissolution mechanism of sulphur in hydrous silicate melts I: assessment of analytical techniques in determining the sulphur speciation in iron-free to iron-poor glasses. Chem Geol 322-323:237–249

Kopylova MG, Matveev S, Raudsepp M (2007) Searching for parental kimberlite melt. Geochim Cosmochim Acta 71:3616-3629

Labidi J, Cartigny P, Moreira M (2013) Non-chondritic sulphur isotope composition of the terrestrial mantle. Nature 501:208-212

Lesne P, Kohn SC, Blundy J, Witham F, Botcharnikov RE, Behrens H (2011) Experimental simulation of closed-system degassing in the system basalt-H_2O-CO_2-S-Cl. J Petrol 52:1737-1762.

Li C, Ripley EM (2009) Sulfur contents at sulfide-liquid or anhydrite saturation in silicate melts: empirical equations and example applications. Econ Geol 104:405-412

McMillan PF (1984) Structural studies of silicate glasses and melts—applications and limitations of Raman spectroscopy. Am Mineral 69:622–644

Mitchell RH (1986) Kimberlites: Mineralogy Geochemistry and Petrology. New York London Plenum press

Morizet Y, Brooker RA, Kohn SC (2002) CO_2 in haplo-phonolite melt: solubility, speciation and carbonate complexation. Geochim Cosmochim Acta 66:1809-1820

Morizet Y, Paris M, Gaillard F, Scaillet B (2010) C–O–H fluid solubility in haplobasalt under reducing conditions: an experimental study. Chem Geol 279:1-16

Morizet Y, Paris M, Di Carlo I, Scaillet B (2013a) Effect of sulfur on the structure of silicate melts under oxidising conditions. Chem Geol 358:131–147

Morizet Y, Brooker RA, Iacono-Marziano G, Kjarsgaard B (2013b) Quantification of CO_2 dissolved in silicate glasses of various compositions with Micro-Raman spectroscopy Am Mineral 98:1788–1802

Morizet Y, Ory S, Di Carlo I, Scaillet B, Echegut P (2015) The effect of Sulphur on the glass transition temperature in anorthite-diopside eutectic glasses. Chem Geol 416:11-18

Morizet Y, Paris M, Sifré D, Di Carlo I, Gaillard F (2017a) The effect of Mg concentration in silicate glasses on CO_2 solubility and solution mechanism: Implication for natural magmatic systems. Geochim Cosmochim Acta 198:115-130

Morizet Y, Gennaro E, Jégo S, Zajacz Z, Iacono-Marziano G, Pichavant M, Di Carlo I, Ferraina C, Lesne P (2017b) A Raman calibration for the quantification of SO_4^{2-} groups dissolved in silicate glasses: Application to natural melt inclusions. Am Mineral 102:2065-2076

Morizet Y, Trcera N, Larre C, Rivoal M, Le Menn E, Vantelon D, Gaillard F (2019) X-ray absorption spectroscopic investigation of the Ca and Mg environments in CO_2-bearing silicate glasses. Chem Geol 510:91-102

Moussallam Y, Morizet Y, Massuyeau M, Laumonier M, Gaillard F (2015) CO_2 solubility in kimberlite melts. Chem Geol 418:198-205

Moussallam Y, Florian P, Corradini D, Morizet Y, Sator N, Vuilleumier R, Guillot B, Iacono-Marziano G, Schmidt BC, Gaillard F (2016) The molecular structure of melts along the carbonatite–kimberlite–basalt compositional joint: CO_2 and polymerization. Earth Planet Sci Lett 434:129-140

Mysen BO (1988) Structure and properties of silicate melts. Development in Geochemistry, vol. 4. Elsevier, Amsterdam

Mysen BO (1990) Effect of pressure, temperature and bulk composition on the structure and species distribution in depolymerised alkali aluminosilicate melts and quenched melts. J Geophys Res B 95:15733-15744

Mysen BO (1999) Structure and properties of magmatic liquids: from haplobasalt to haploandesite. Geochim Cosmochim Acta 63:95-112

Nowicki T, Crawford B, Dyck D, Carlson J, McElroy R, Oshurst P, Helmstaedt H (2004) The geology of kimberlite pipes of the Ekati property, Northwest territories, Canada. Lithos 76:1-27.

O'Neill HSC, Mavrogenes JA (2002) The sulfide capacity and the sulfur content at sulfide saturation of silicate melts at 1400 °C and 1 bar. J Petrol 43:1049-1087

Palme H, O'Neill HSC (2003) Cosmochemical estimates of mantle composition. In Carlson RW (ed) Treatrise on Geochemistry 2:1-38

Pawley AR, Holloway JR, McMillan PF (1992) The effect of oxygen fugacity on the solubility of carbon–oxygen fluids in basaltic melt. Earth Planet Sci Lett 110:213-225

Pearson DG, Shirey SB, Harris JW, Carlson RW (1996) Sulphide inclusions in diamonds from the Koffiefontein kimberlite, S Africa: constraints on diamond ages and mantle Re–Os systematics. Earth Planet Sci Lett 160:311-326

Pearson DG, Shirey SB, Harris JW, Carlson RW (1998) Sulphide inclusions in diamonds from the Koffiefontein kimberlite, S Africa: constraints on diamond ages and mantle Re–Os systematics. Earth Planet Science Lett 160:311-326

Presnall DC, Gudfinnsson GH (2005) Carbonate-rich melts in the oceanic low-velocity zone and deep mantle. Geol Soc Am Spec Pap 388:207-216

Rudnick RL, Eldridge CS, Bulanova GP (1993) Diamond growth history from in situ measurement of Pb and S isotopic compositions of sulphide inclusions. Geology 21:13-16.

Scaillet B, Pichavant,M (2005) A model of sulphur solubility for hydrous mafic melts: application to the determination of magmatic fluid compositions of Italian volcanoes. Ann Geophys 48:671-697

Shi P, Saxena SK (1992) Thermodynamic modeling of the C-H-O-S fluid system. Am Mineral 77:1038-1049

Sobolev NV, Kaminsky FV, Griffin WL, Yefimova ES, Win TT, Ryan CG, Botkunov AI (1997) Mineral inclusions in diamonds from the Sputnik kimberlite pipe, Yakutia. Lithos 39:135-157

Tappe S, Smart K, Torsvik T, Massuyeau M de Wit M (2018) Geodynamics of kimberlites on a cooling Earth: Clues to plate tectonic evolution and deep volatile cycles. Earth Planet Sci Lett 484:1-14

Thibault Y, Holloway JR (1994) Solubility of CO_2 in a Ca-rich leucitite: Effects of pressure temperature and oxygen fugacity Contrib Min Pet 116:216-224

Wallace ME, Green DH (1988) An experimental determination of primary carbonatite magma composition. Nature 335:343-346

Wendlant RF (1982) Sulfide saturation of basalt and andesite melts at high pressures and temperatures. Am Mineral 67:877-885

Wetzel DT, Rutherford MJ, Jacobsen SD, Hauri EH, Saal AE (2013) Degassing of reduced carbon from planetary basalts. Proc Nat Acad Sci 110:8010-8013

Wilke M, Klimm K, Kohn SC (2011) Spectroscopic studies on sulfur speciation in synthetic and natural glasses. In H. Behrens and J.D. Webster, Eds., Sulfur in Magmas and Melts: Its Importance for Natural and Technical Processes. Reviews in Mineralogy and Geochemistry, Mineralogical Society of America 73:41–78.

Zajacz Z (2015) The effect of melt composition on the partitioning of oxidized sulfur between silicate melts and magmatic volatiles Geochim Cosmochim Acta 158:223-244

Zajacz Z, Tsay A (2019) An accurate model to predict sulfur concentration at anhydrite saturation in silicate melts. Geochim Cosmochim Acta 261:288-304

Table caption

Table 1 Experimental conditions, major elements compositions, volatile content and fluid phase composition.

	HK^{th*}	HK-2*	HK-3*	HK-1*	HKS1-2	HKS1-3	HKS2-3	HKS1-1	HKS3-1	HKS4-1	HKS2-2	HKS3-2	HKS4-2
P (GPa)	–	0.5	1	1.5	0.5	0.5	0.5	1	1	1	1.5	2	2
T (°C)	–	1525	1525	1525	1525	1525	1525	1525	1500	1500	1525	1500	1500
ppm S^{init}	–	0	0	0	12800	12800	6500	12800	24000	3300	6500	24000	3300
wt% CO_2^{init}	–	17.7	17.7	17.7	18.3	18.3	19.5	18.3	17.2	20.2	19.5	17.2	20.2
wt% SiO_2	44.5	40.1	37.2	40.2	37.3	37.2	36.3	39.0	38.6	38.0	37.0	33.6	35.3
Al_2O_3	4.9	4.4	4.2	4.3	4.3	4.3	4.2	5.5	3.1	3.7	4.2	3.7	3.7
MgO	22.8	21.3	21.8	21.9	18.6	18.6	18.4	18.9	17.9	19.0	18.8	16.6	17.1
CaO	22.8	22.3	21.4	22.0	26.9	27.0	26.2	24.7	25.7	24.4	26.7	24.7	25.1
Na_2O	4.9	4.5	4.5	4.5	3.8	4.0	4.0	3.1	3.5	4.2	4.1	3.7	3.8
SO_2	–	–	–	–	2.2	2.1	1.1	0.6	1.8	0.1	1.0	4.4	0.5
Total	99.9	92.7	89.1	92.9	93.1	93.2	90.2	91.9	90.7	89.5	91.9	86.8	85.5
NBO/T†	2.4	2.2	2.3	2.2	2.4	2.4	2.4	2.1	2.3	2.3	2.4	2.4	2.4
wt% $CO_2^{\ddagger}$	–	2.9	5.6	7.1	3.5±0.3	3.1±0.6	5.0±0.1	6.8±0.2	4.2±0.1	5.9±0.2	7.9±0.5	10.9±0.1	11.3±0.8
ppm $S^{6+\ddagger}$	–	–	–	–	13402±1194	11484±336	7906±34	4161±25	11312±192	n.d.	7706±98	21296±1364	2112±236
ppm $S^{tot\ddagger}$	–	–	–	–	11979±676	11298±514	6168±565	3393±323	9970±578	536±189	5620±443	25507±851	2870±221
$XSO_2^{fl\S}$	–	0	0	0	~0	~0	~0	0.05	0.07	0.01	~0	~0	~0
$XCO_2^{fl\S}$	–	1	1	1	~1.0	~1.0	~1.0	0.95	0.93	0.99	~1.0	~1.0	~1.0
$fSO_2^{\S}$	–	0	0	0	~0	~0	~0	5030	6713	1462	~0	~0	~0
$fCO_2^{\S}$	–	13233	86643	332516	~13233	~13233	~13233	82436	81029	85420	~332516	~1162262	~1162262

* The haplokimberlite theoretical composition is the one reported in Morizet et al. (2017a). The HK-1 -2 and -3 are from Morizet et al. (2017a) and are for S-free experiments.

† The NBO/T is the degree of polymerization expressed as the ratio between Non-Bridging Oxygen and Tetrahedra and is calculated form major element concentrations (see Brooker et al. 2001).

‡ The wt% CO_2 and ppm S^{6+} are determined from the deconvolution of the Raman spectra and using the subsequent calibrations of Morizet et al. (2013b, 2017b). The ppm S^{tot} is determined from the EPMA analyses. The error on the values is ~10% in relative to the value for volatiles determined using Raman deconvolution. The error on the ppm S^{tot} is determined from the standard deviation on more than 20 analyses.

§ The fluid phase composition is estimated from mass balance calculation (see text for details). The volatile fugacity is determined from the equation of state of Holland and Powell (1991) and Shi and Saxena (1991) for CO_2 and SO_2, respectively. Considering that S is almost entirely dissolved in the melt, the activity of SO_2 in the fluid phase is therefore close to 0.

Figure caption

Fig. 1 a) Raman spectra obtained for HKS glasses synthesized at different pressures. The spectra are scaled to the intensity of the ν_1 CO_3^{2-} peak. b) Typical Raman spectrum deconvolution for HKS3-2 glass: one peak for CO_3^{2-}, one peak for SO_4^{2-} and four peaks for the silicate network. The wt% CO_2 and ppm S^{6+} is determined from the deconvolution and subsequent calibrations: Morizet et al. (2013b, 2017b).

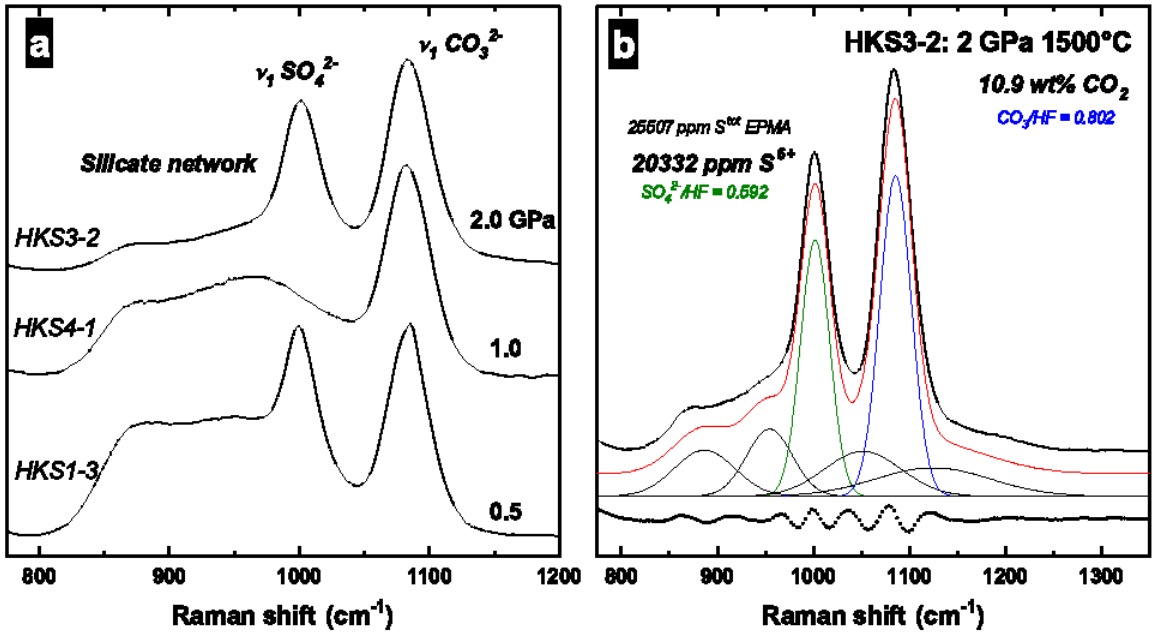

Fig. 2 S content determined by Raman spectroscopy (ppm S^{6+}) and the calibration of Morizet et al. (2017b) from the Raman spectrum simulations (see Fig. 2) as a function of S content determined by EPMA. The reported errors are the ones in Table 1 and obtained from standard deviation of the replicated analyses.

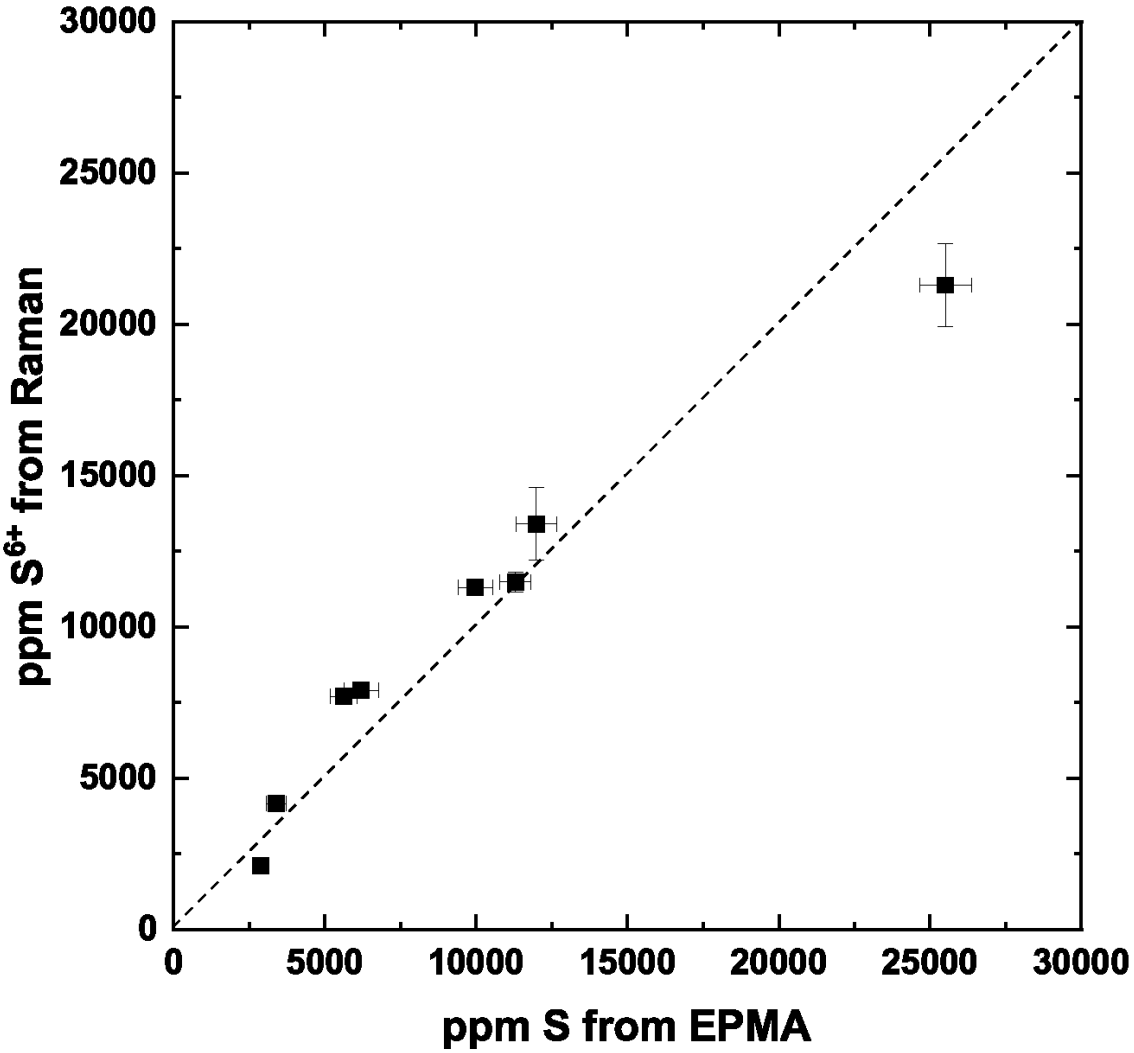

Fig. 3 Change in wt% CO_2 and ppm S^{tot} as a function of pressure. A trend has been added for CO_2 showing the increase in CO_2 solubility as a function of pressure. S-bearing and S-free data are reported.

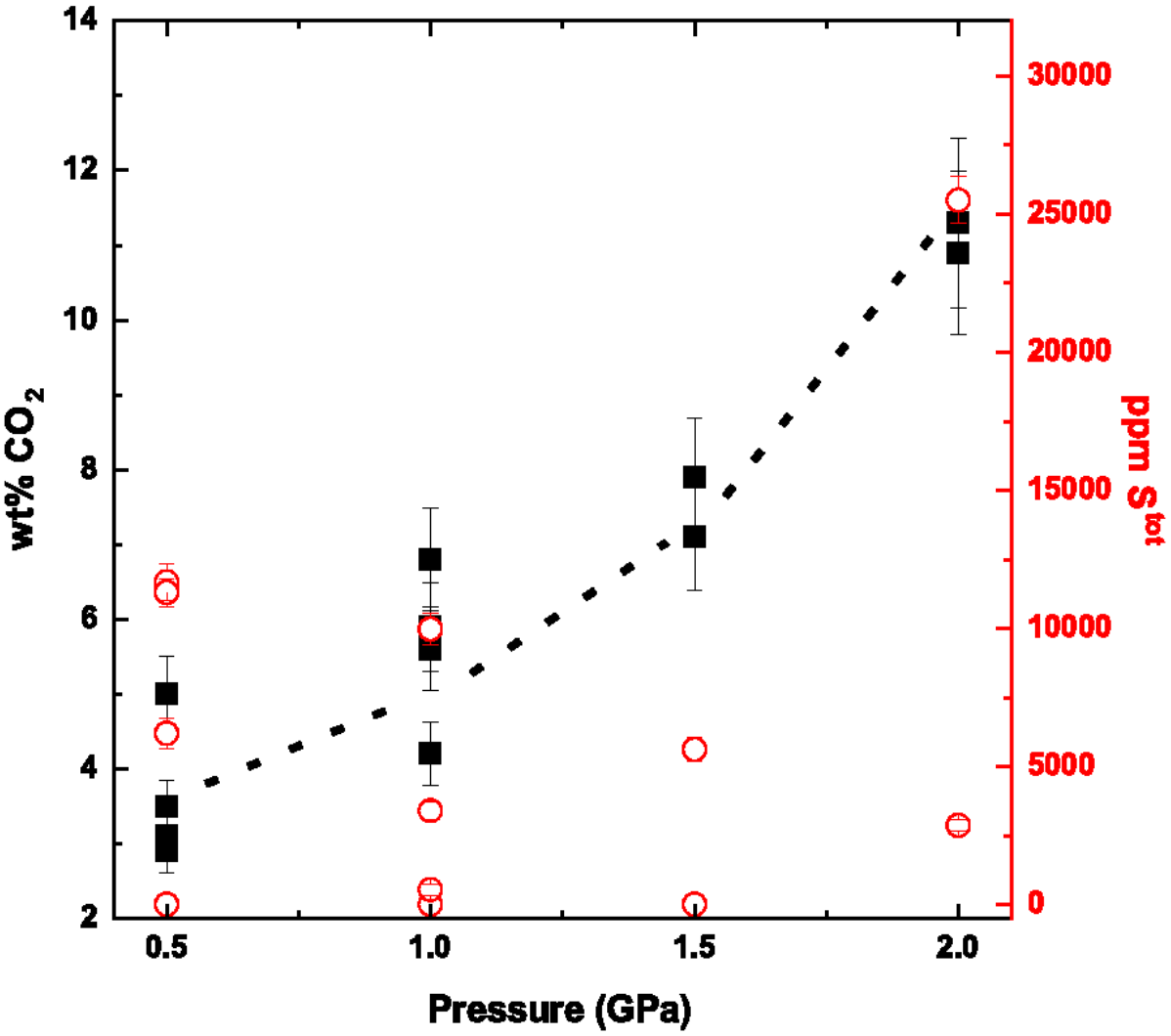

Fig. 4 Change in CO_2 solubility as a function of calculated f_{CO2}(P,T). Data from Brey and Ryabchikov (1994), Brooker et al. (2001), Thibault and Holloway (1994) and Morizet et al. (2017a) are also shown for comparison.

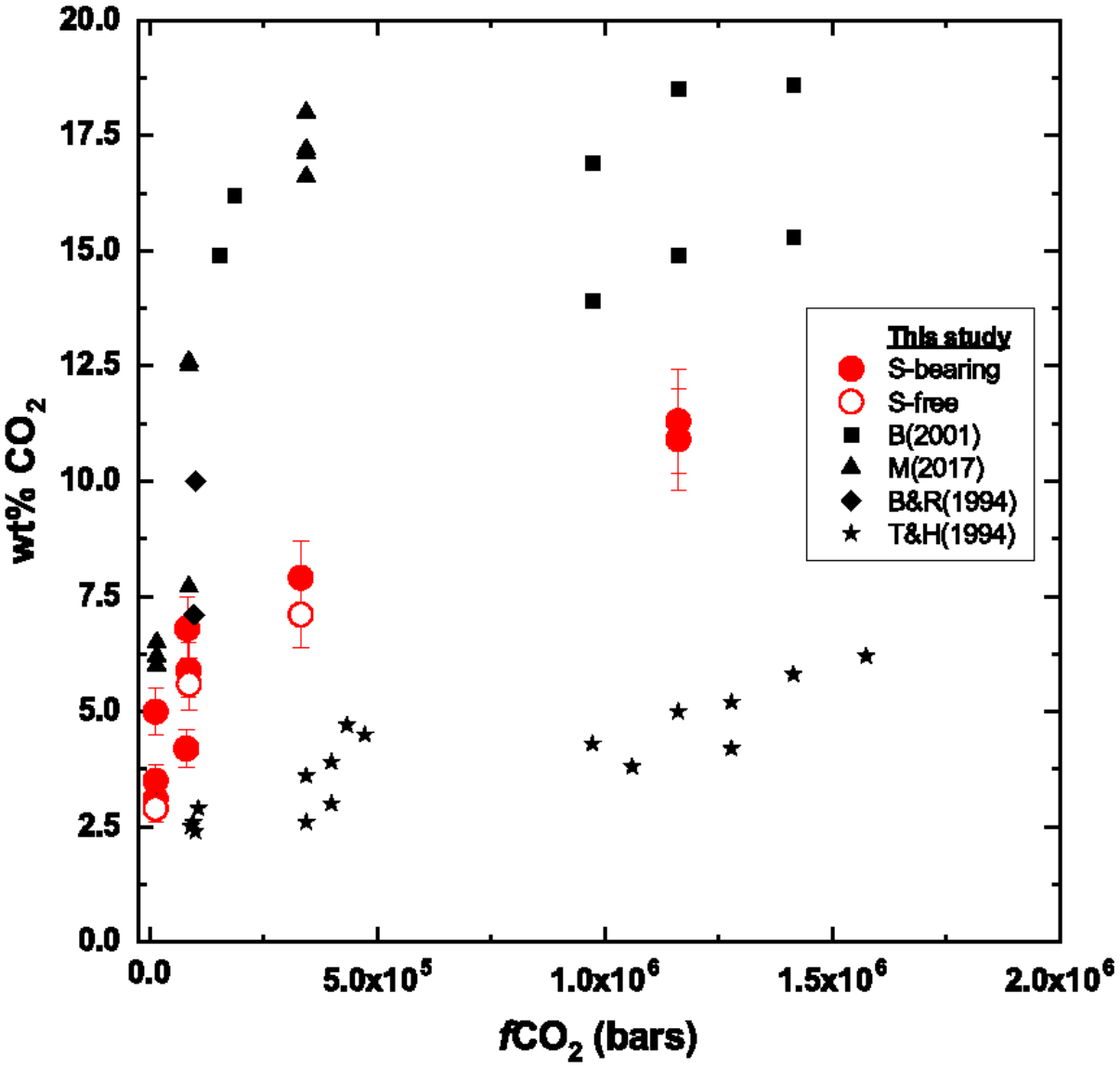

SUPPLEMENTARY INFORMATION

Secondary Electron Microscopy

The HKS3-2 glass sample exhibits the highest S content; which is measured at 25507±851 ppm S by EPMA. Such high S content was surprising as it represents the highest dissolved S in silicate glasses so far. We observe this glass sample with SEM in backscattered in order to investigate the possible chemical heterogeneities. The images on Fig. 5 obtained on two different glass chips from the experimental charge show that the HKS3-2 glass sample is entirely homogeneous in composition and not evidence of crystalline sulfate is observed. Considering that the measured S content is close to the initially loaded S content and that no evidence for crystalline sulfate indicating sulfate saturation is found; the S solubility is not reached and that the amount of S that can be dissolved in this type of depolymerized composition is higher than 2.5 wt%.

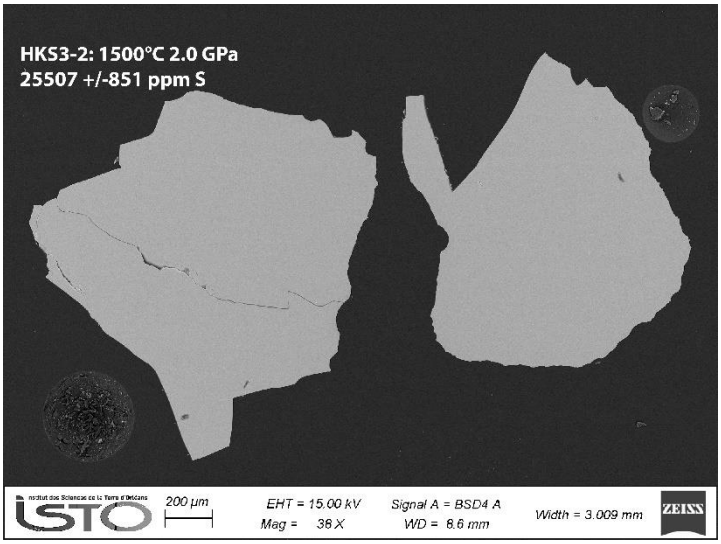

Fig. 5 Scanning Electron Microscopy image acquired in Backscattered mode for two glass chips of HKS3-2 synthesised at 2.0 GPa and 1500°C with an initial S content of ~24000 ppm. The SEM picture reveals that the glass is totally homogeneous in composition and that sulfate saturation is not reached.

Raman spectrum deconvolution

Typical Raman spectrum deconvolutions are shown in Fig. 6 for the investigated S- and CO_2-bearing glass samples. The raw Raman spectra are first treated to subtract the baseline using a polynomial function (3 or 4 order) with anchors points at ~200, ~800 and ~1200 cm^{-1}, respectively. These areas are chosen as they are no signal areas.

The deconvolution is conducted on the high frequency region corresponding the symmetric stretch of the silicate network (Q^n species), the symmetric stretch of the sulfate groups (ν_1 SO_4^{2-}) and the symmetric stretch of the carbonate groups (ν_1 CO_3^{2-}). The simulation is performed with the Gauss function in Origin 7.5© using 4 Gaussian lines for the silicate network, 1 Gaussian line for the SO_4^{2-} and 1 Gaussian line for the CO_3^{2-}.

For most of the spectrum, the initial parametrization (i.e. peak position) was as follow: 1000 cm^{-1} for ν_1 SO_4^{2-}, 1085 cm^{-1} for ν_1 CO_3^{2-}, 880, 910, 950, 1050 cm^{-1} for the silicate network. However, in a few cases (for high CO_2 and S contents), it was required to add a Gaussian contribution at ~1100 cm^{-1}. Although the question of the effect of volatile species on the silicate melt structure is not the purpose of this work, it has been demonstrated that the dissolution of volatiles induces a polymerization of the silicate network (Moussallam et al. 2016; Morizet et al. 2013, 2017); which will be visible on the Raman spectrum by a shift in the high frequency towards higher Raman shift and appearance of additional peaks such as the one at 1100 cm^{-1}. It should be emphasised that the initial peak positions are consistent with previous works (see Rossano and Mysen 2013; and reference therein).

The FWHM (Full Width at Half Maximum) is set initially at 30 cm^{-1} for the ν_1 SO_4^{2-} and the ν_1 CO_3^{2-}; 55 cm^{-1} for the silicate network peaks.

The optimization is done in several steps. First, the position of the peaks is optimized at a fixed FWHM; then the FWHM is optimized at the fixed position. These two steps are repeated several times until the fit has totally converged and that the chi-square (χ^2) is as low as possible. The χ^2 represents the goodness and robustness of the fit; however, one should keep in mind that the proposed fit represents only one possible solution. The residuals shown in Fig. 6 suggest that the fits are reliable, though. The derived parameters are reported in Table 2. The ν_1 SO_4^{2-}/HF and ν_1 CO_3^{2-}/HF ratios are calculated from the derived area of each peak and shown in Table 2 along with the standard deviation obtained from the simulation of several Raman spectra.

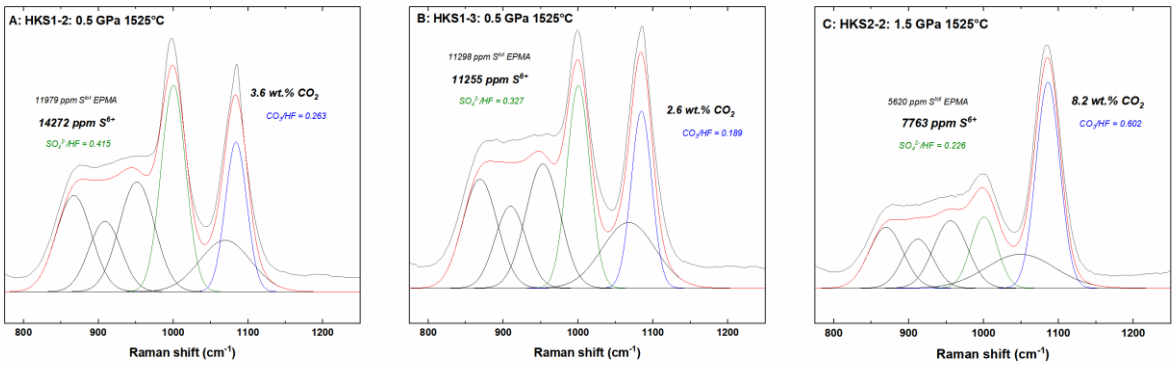

Fig. 6 Typical Raman spectrum deconvolution obtained for HKS1-1 (A), HKS1-3 (B), HKS2-2 (C). The peak for ν_1 CO_3^{2-} and SO_4^{2-} are indicated in blue and green, respectively. The ratios to quantify both the CO_2 and the S^{6+} are reported and calculated using the areas of the ν_1 CO_3^{2-} and SO_4^{2-} peaks divided by the areas of the peaks for the silicate network (in black).

References

Moussallam Y, Florian P, Corradini D, Morizet Y, Sator N, Vuilleumier R, Guillot B, Iacono-Marziano G, Schmidt BC, Gaillard F (2016) The molecular structure of melts along the carbonatite–kimberlite–basalt compositional joint: CO_2 and polymerization. Earth Planet Sci Lett 434:129–140

Morizet Y, Paris M, Di Carlo I, Scaillet B (2013) Effect of sulfur on the structure of silicate melts under oxidising conditions. Chem Geol 358:131–147.

Morizet Y, Paris M, Sifré D, Di Carlo I, Ory S, Gaillard F (2017) Towards the reconciliation of viscosity change and CO_2-induced polymerization in silicate melts. Chem Geol 458:38–47.

Rossano S, Mysen BO (2013) Raman spectroscopy of silicate glasses and melts in geological system. In J Dubessy, MC Caumon and F Rull, Eds., Raman Spectroscopy Applied to Earth Sciences and Cultural Heritage. EMU Notes in Mineralogy, 12:321–366.

Table 2 Simulation results for the HKS Raman spectra.

Vibration	Parameter*	HKS1-2	HKS1-3	HKS2-3	HKS1-1	HKS3-1	HKS4-1	HKS2-2	HKS3-2	HKS4-2
Number of spectra		3	4	5	3	5	9	5	2	4
ν_1 SO_4^{2-}	Position	1000.2	1000.4	997.3	1003.1	1000.0	1005.7	1000.5	1001.7	1007.8
	FWHM	32.7	30.5	36.1	36.0	34.9	33.6	34.6	30.3	35.9
ν_1 CO_3^{2-}	Position	1084.0	1084.6	1084.4	1086.8	1089.2	1085.5	1085.9	1085.5	1085.9
	FWHM	28.50785	27.30133	30.72	32.5	33.9	33.5	31.9	32.9	34.7
Silicate network	Position	1069.3	1067.5	1054.7	1049.4	1054.2	1050.9	1049.1	1124.2	1044.0
	FWHM	68.1	70.6	73.6	86.6	76.4	69.6	91.5	120.1	100.3
	Position	951.4	953.0	950.4	962.0	951.7	981.3	955.8	1051.4	974.9
	FWHM	47.3	45.9	51.0	57.7	50.8	60.2	45.4	79.7	64.4
	Position	908.8	909.7	902.7	906.0	904.7	934.7	912.3	954.3	915.2
	FWHM	43.1	41.2	45.0	56.4	42.9	58.1	40.6	47.8	76.5
	Position	867.0	868.9	864.2	864.7	867.5	874.5	869.6	886.6	848.2
	FWHM	47.1	46.2	43.6	39.3	42.1	54.1	45.3	63.0	76.0

ν_1 SO_4^{2-}/HF†	0.390± 0.035	0.334± 0.010	0.230± 0.001	0.121± 0.001	0.329± 0.006	0.013± 0.002	0.224± 0.003	0.620± 0.040	0.061± 0.007
ν_1 CO_3^{2-}/HF†	0.256± 0.019	0.227± 0.045	0.369± 0.003	0.499± 0.016	0.309± 0.004	0.434± 0.012	0.580± 0.036	0.799± 0.004	0.836± 0.060

* The determined parameters are the peak position and the Full Width at Half Maximum (FWHM).
† The ratios between ν_1 SO_4^{2-}/HF and ν_1 CO_3^{2-}/HF are determined from the derived areas of the peaks. The HF value is obtained by summing the peak areas of the silicate network Gaussian lines. The error on the ratio corresponds to the standard deviation of the ratio determined from the different Raman spectra simulation.